Nanoscale



PAPER

View Article Online
View Journal | View Issue



Cite this: Nanoscale, 2022, 14, 17985

Controlling morphology in electrosprayed methylcellulose nanowires *via* nanoparticle addition: coarse-grained modeling and experiments†

Jonathan M. Blisko, [©] ^a Michael J. Grzenda, [©] ^b Rachel M. Vladimirsky, [©] ^c Christopher E. Shuck, [©] ^d Jonathan P. Singer [©] * ^{b,c} and Xin Yong [©] * ^a

Electrospray deposition (ESD) has shown great promise for manufacturing micro- and nanostructured coatings at scale on versatile substrates with complex geometries. ESD exhibits a broad spectrum of morphologies depending upon the properties of spray fluids. Among them are nanowire forests or foams obtained *via* the in-air gelation of electrospray droplets formed from methylcellulose (MC) solutions. In this study, we explored MC ESD loaded with nanoparticles of various shapes and uncovered the effects of particle fillers on morphology evolution using coarse-grained simulations and physical experiments. Utilizing electrostatic dissipative particle dynamics, we modeled the electrohydrodynamic deformation of particle-laden MC droplets undergoing in-flight evaporation. The simulations quantitatively predict the suppression of droplet deformation as the size or concentration of spherical nanoparticles increases. While small particles can be readily encapsulated into the nanowire body, large particles can arrest nanowire formation. The model was extended to nanoparticles with complex topologies, showing MC nanowires emerging from particle edges and vertices due to curvature-enhanced electric stress. In all cases, strong agreements were found between simulation and experimental results. These results demonstrate the efficacy of the coarse-grained model in predicting the morphology evolution of electrosprayed droplets and lay the groundwork for employing MC nanowires for developing nanostructured composites.

Received 28th July 2022, Accepted 15th November 2022 DOI: 10.1039/d2nr04177d

rsc.li/nanoscale

Introduction

There is a significant and growing need for high-precision and high-throughput manufacturing that stimulates not only the development of new techniques but also the repurposing of existing methods. Although primarily employed as an analytical tool, electrospray deposition (ESD) has been increasingly admitted as a manufacturing method over the past decade. ¹⁻³ ESD applies strong electric fields to generate monodisperse droplets from solutions/dispersions and drive them toward grounded targets. This method allows the deposition of versatile types of materials at nanograms per droplet into complex

ESD of polymer solutions produces deposits with rich morphologies depending on the properties of the solution. The morphology evolution is governed by the complex interplay of viscous force, surface tension, and electric stress as the droplet undergoes evaporation and Coulombic fission in flight. In addition, the spray of insulating polymers produces thicknesslimited films in which the charge accumulation repels incoming spray droplets. 4,11,12 This self-limiting behavior enables the conformal coating of complex 3D surfaces. 13 Recent work from our group has shown that methylcellulose (MC) forms a selflimiting coating with a unique nanowire architecture when processed by ESD from water: ethanol solutions.7 This morphology presents an intermediate spray regime between the electrospinning of wire mats and particulate sprays. As part of this prior work, it was demonstrated that the nanowires are formed via drop-by-drop electrospinning of MC gels. The

²D and 3D micro- and nanostructures.⁴⁻⁷ The relative simplicity and low cost of ESD also aid in the popularity of its use in various applications. Specifically, ESD has been used in the fabrication of microscale electronic devices, drug coating for improved longevity of release characteristics, and the encapsulation of compounds for use in food.⁸⁻¹⁰

^aDepartment of Mechanical Engineering, Binghamton University, Binghamton, New York 13902, USA. E-mail: xyong@binghamton.edu

^bDepartment of Materials Science Engineering, Rutgers University, Piscataway, New Jersey 08854, USA. E-mail: jonathan.singer@rutgers.edu

^cDepartment of Mechanical and Aerospace Engineering, Rutgers University, Piscataway, New Jersey 08854, USA

^dA.J. Drexel Nanomaterials Institute, Drexel University, Philadelphia, Pennsylvania 19104 - USA

[†] Electronic supplementary information (ESI) available. See DOI: https://doi.org/10.1039/d2nr04177d

Paper Nanoscale

homogeneous gelation of MC is enhanced by significant shear forces and surface charge during the ESD process. The formation of nanowires on an individual droplet level eventually creates a highly porous, low-density forest or foam as deposition continues.

To further elucidate the physical mechanisms of nanowire formation, this study explores the interaction of nanoparticles (NP) with MC during gelation by combining computer simulations and experiments. Theoretical modeling and numerical simulations have been widely used for understanding continuous nanowire formation in electrospinning. ¹⁴ However, the effects of NP addition on the electrohydrodynamic deformation of individual polymer droplets remain unexplored. The spray of polymer nanocomposites provides new opportunities for manipulating the ESD process and expanding the functionalities of deposits. Previous studies have shown the ESD deposition of single and isolated gold NPs, demonstrating an ability to control the number of NPs within a sprayed droplet. 15 Due to its homogeneous gelation behavior, using MC as the host material allows us to delineate the effect of immobile fillers on the dynamics of nanowire formation. The nanowire structure also efficiently separates and isolates particles, potentially achieving high particle loadings beyond the percolation limit for random packing. Moreover, the inclusion of NPs allows additional control over the local viscosity and the droplet dynamics.

Here, we hypothesize that the immobile domains of NPs guide the droplet evolution and the final morphology depends on the fillers' relative size, volume fraction, and geometry. To test this hypothesis, we conducted coarse-grained simulations of the ESD of particle-laden MC droplets (see Fig. S1† for an example). The simulations predict the morphology evolution of droplets with single and multiple embedded particles, representing dilute and concentrated regimes. The effects of particle curvature were further assessed. The experiments were performed to validate the modeling predictions by incorporating water-dispersible spherical silica particles and 2D Ti₃C₂T_x MXene flakes¹⁶ with sizes ranging across approximately one order of magnitude into the spray solution.

Methods

Computer simulations

Electrostatic dissipative particle dynamics. The electrostatic dissipative particle dynamics (eDPD) method simulates the electrohydrodynamics of complex fluids on the mesoscale by aggressively coarse-graining solid/fluid components in groups of spherical beads. This approach allows one to simulate significantly larger systems than molecular dynamics, which is necessary for meaningful comparison against experiments. The dynamics for each bead i are governed by Newton's laws: $\frac{d\mathbf{r}_i}{dt} = \mathbf{v}_i$ and $m \frac{d\mathbf{v}_i}{dt} = \mathbf{f}_i$. Integration of these equations is done using a velocity-Verlet algorithm. The force f_i captures physical interactions between components in a multiphase system, composed of nonbonded and bonded forces.

The nonbonded components are the conservative, dissipative, random, and electrostatic forces given by $\mathbf{F}_{ii}^{\text{C}}$, $\mathbf{F}_{ii}^{\text{D}}$, $\mathbf{F}_{ii}^{\text{R}}$, and $\mathbf{F}_{i}^{\mathrm{E}}$, respectively. In particular, the conservative force is defined *via* a soft-core repulsion given by $\mathbf{F}_{ii}^{\mathrm{C}} = a_{ij}(1 - r_{ij}/r_{\mathrm{c}})\hat{\mathbf{r}}_{ij}$ for $r_{ij} < r_{\mathrm{c}}$, with $r_{ij} = |\mathbf{r}_i - \mathbf{r}_j|$, $\hat{\mathbf{r}}_{ij} = (\mathbf{r}_i - \mathbf{r}_j)/r_{ij}$, and r_c being a cutoff radius. The interaction parameter, $a_{ij} > 0$, depends upon the type of the two interacting beads and can be correlated to the fluid compressibility and the interfacial tension between immiscible fluids. The dissipative force is proportional to the relative velocity $v_{ii} = |\mathbf{v}_i - \mathbf{v}_i|$, given by $\mathbf{F}_{ii}^{\mathrm{D}} = -\gamma (1 - r_{ij}/r_{\mathrm{c}})^2 (\mathbf{r}_{ij} \cdot \mathbf{v}_{ij}) \hat{\mathbf{r}}_{ij}$. Here, γ is a friction coefficient. Finally, the random force employs a Gaussian random number θ with zero mean and unit variance such that $\mathbf{F}_{ii}^{\mathrm{R}} = \sigma (1 - r_{ij}/r_{\mathrm{c}})\theta(\Delta t)^{-1/2}\hat{\mathbf{r}}_{ij}$. The noise strength σ is related to γ via the fluctuation-dissipation theorem, which gives $\sigma = \sqrt{2k_{\rm B}T\gamma}$. These nonbonded forces on the reference bead i are calculated for neighbor beads within the cutoff radius r_c . Notably, the conservative, dissipative, and random forces are all pairwise for conserving momentum and capturing hydrodynamics. 18 The details of the electrostatic force will be described below. A harmonic bond force $\mathbf{F}_{ii}^{\mathrm{B}} = -k(\mathbf{r}_{ij} - b)\hat{\mathbf{r}}_{ij}$ is included for modeling polymer chain connectivity, where k is the spring constant and b is the equilibrium distance. Thus, the total force on each bead is represented by $\mathbf{f}_i = \sum\limits_{j \neq i} (\mathbf{F}^{\text{C}}_{ij} + \mathbf{F}^{\text{D}}_{ij} + \mathbf{F}^{\text{R}}_{ij}) + \sum\limits_{j \neq i} \mathbf{F}^{\text{B}}_{ij} + \mathbf{F}^{\text{E}}_{i}$. Per convention, the simu-

lation results are presented in reduced units with r_c , m, k_BT , and the characteristic time $\tau = \sqrt{mr_{\rm c}^2/k_{\rm B}T}$ all set to unity. The friction coefficient γ and the random force amplitude σ are 4.5 and 3.0 for all bead type pairs, respectively.

In order to model the net charge imparted by ESD, explicit ion beads are initially distributed throughout the droplet randomly. Electrostatic interactions between these charged beads are resolved using Groot's method. 19 Compared to the Ewald sum, 20,21 another popular technique for solving electrostatic interactions, the Groot method is capable of simulating different dielectric media. The electrostatic solver was implemented in parallel as an in-house module of LAMMPS, and the details have been described previously. 22-24 Evaporation of droplets is simulated phenomenologically by homogeneous removal of solvent beads from the entire droplet at a rate of 20 beads per 10 timesteps. This rate is chosen based on a systematic study conducted in our previous work,⁷ which compares the effect of homogeneous removal with a physical evaporation scheme, in which the solvent beads are only removed at the droplet surface. The results show that the homogeneous removal and physical evaporation produce the same homogeneous increase in polymer density in the droplet at an equivalent rate of 2 beads per 1 time step. The homogeneous removal at this low rate thus models rapid gelation of an MC polymer network that uniformly increases the droplet viscosity. The polymer is considered to be solidified when evaporation completes, resulting in the final morphology of the sprayed droplet. Gas beads are added near the boundary of the simulation box to maintain fluid incompressibility. 17

Particle-laden droplets. As in our previous studies, ⁷ a linear MC polymer is modeled as a string of 200 connected beads. The bond force parameters k = 64 and b = 0.5 are used for minimizing unphysical bond crossing and reproducing correct polymer rheology. Critical for this study is the inclusion of rigid NPs within the droplet as it undergoes evaporation and Coulombic fission. Each NP is constructed by carving a face-centered cubic (FCC) cluster (with a lattice constant a = 0.87) of beads into specific shapes. The NPs are restrained as rigid bodies such that the relative positions of the constituent beads do not change.

Each simulation includes a droplet of mixed polymer beads, solvent beads, and NPs. The initial radius of the droplet is approximately 12. The initial composition of the fluid phase of the droplet is 30% (v/v) polymer beads and 70% (v/v) solvent. The polymers initially adopt random conformations. The ion bead concentration is set to 1.35% (v/v) to ensure no droplet deformation occurs without solvent evaporation. NPs are randomly distributed throughout the droplet initially (Fig. S1 \dagger). Notably, the surface charge of NPs is not considered in this study. Outside the droplet, gas beads fill the remaining volume of the simulation box.

Simulation setup. Consistent with typical DPD simulations, the average number density of the whole system is set to 3. The simulation first runs 3000 time steps in the absence of electrostatic interactions for the equilibration of the droplet; in particular the relaxation of polymer chains. The equilibration is followed by up to 7600 time steps of evaporation with electrostatics. The magnitude of the simulation time step is set to 0.04. For each particle size, concentration, and shape, we conduct multiple simulations with independently generated initial configurations and different random seeds, allowing us to obtain droplet deformation statistics.

The periodic boundary conditions require charge neutrality of the entire system to ensure finite electrostatic potential energy theoretically. In order to balance charged beads in the droplet, an equal number of oppositely charged beads of the same charge magnitude are introduced randomly near the boundary of the simulation box. These counterions effectively screen the electrostatic interactions between periodic images. The simulation box dimensions are set to 100 by 100 by 100, large enough to minimize the effect of boundary counterions on droplet dynamics. We compare particle-free droplet dynamics in the simulation systems with and without counterions (i.e., charge neutrality). Fig. S2† demonstrates that the droplets in the two systems show consistent deformation. The inclusion of counterions on the boundary of the simulation domain does not significantly alter the morphology evolution. The quantitative difference in the radius of gyration and relative shape anisotropy (Fig. S3a and b†) can be attributed to more homogeneous nanowire formation when the boundary counterions are present. The more rapid and pronounced growth is promoted by a stronger background electric field induced by the counterions. However, the effective diameters of the nanowires remain highly consistent between the two systems (Fig. S3c†). This comparison indicates that the droplet dynamics are dominated by charges concentrated in the center droplet. The electrostatic interactions with periodic images

have no qualitative effects on the droplet deformation due to the large box size, regardless of whether screened by the boundary counterions.

The DPD interaction parameters between beads of the same type are set to 25 per convention.¹⁷ The cross-species interaction parameters for components in the droplet are all 25 to model a well-mixed solution of polymer chains and NPs that is sprayed. To capture the droplet surface tension, the interaction parameters between the gas beads and solvent, polymer, and NP beads are set to 100. An interaction strength of 1000 is used between the gas and ion beads to ensure no ion ejection at the early evaporation stage. Although the counterions at the boundary are not expected to have direct DPD interactions with the droplet components, the relevant interaction parameters are also 1000, similar to the ion-gas interaction parameter. The relative permittivities of the droplet and gas phases are set to 0.01 and 1 to capture the dielectric contrast across the droplet surface. The charge for each ion bead is 0.5, while the counterion has a charge of -0.5 to maintain the net charge neutrality of the system.

The total number of DPD beads in the simulation is 3×10^6 . According to the variations in the size and number of NPs, the ranges of beads of different types were $13\,301-15\,192$ solvent beads, 5800-6600 polymer beads, 257-293 ion beads, and 19-5425 rigid particle beads. The remains are gas beads. Correspondingly, the number of MC polymer chains in the droplet ranges from 29 to 33. This results in an effective ratio of ions to polymer chains to be approximately 8.9 ions per chain. Notably, this number merely represents an effective charge concentration as the polymer chains are neutral and contain no charged beads.

Experiments

Materials

Methylcellulose (15 cP) was used as received from Sigma Aldrich. Aqueous dispersions of silica nanosphere (labeled 50 nm, 200 nm, and 500 nm and measured through 10 SEM measurements to be 70 \pm 4 nm, 210 \pm 10 nm, and 450 \pm 40 nm, respectively) were purchased from Alpha Nanotech Inc. Ti₃C₂T_x MXene was prepared by etching Ti₃AlC₂ (Carbon Ukraine, <40 micron) in a mixture of HF (Acros International, 49 wt%), HCl (Fisher Scientific, 12.1 M), and deionized water (DI; 15 M Ω resistance) at an etchant volumetric ratio of 2:6:12 HF:H₂O:HCl, as described previously.²⁸ The Ti₃AlC₂ powder was slowly added into the etchant over the course of 10 min. This was stirred at 300 rpm for 24 h at 35 °C. Following this, the $Ti_3C_2T_x$ was washed to neutral by repeated centrifugation. The neutral Ti₃C₂T_x was then added into 20 mL DI water, then 1 g LiCl (99%, Alfa Aesar) was added to delaminate the MXene. This was stirred at 300 rpm for 24 h at 35 °C. Following this, the MXene was collected by centrifugation. Briefly, the mixture was centrifuged at 3500 rpm for 15 minutes. For the first few cycles, the supernatant was clear, and was thus discarded. Afterwards, fresh DI water was added

Paper Nanoscale

to the sediment, and it was fully redispersed. This was repeated until the supernatant was black, whereby the black supernatant was collected instead of discarded. This process was continued until the supernatant was again clear. Afterwards, the MXene solution was concentrated to 2 wt% by centrifuging the collected Ti₃C₂T_x at 10 000 rpm for 10 min. P-type Si wafers (0–100 Ω cm) were purchased from University Wafer Inc. To make the spray solutions, MC was mixed directly into either the aqueous particle dispersion or DI water and left to fully dissolve overnight. To achieve stable electrospray, ethanol was mixed with the aqueous solutions at a weight ratio of 60:40 water to ethanol. The MC concentration was kept at either 1% or 0.25% by weight with respect to the waterethanol mixture. Particles were sprayed both with and without MC. Without MC, the ethanol was added directly to the dispersion resulting in a concentration of 0.6 wt% for the silica and 1.2 wt% for the MXene. With MC, the MXene particles were sprayed in 1 wt% MC and the MXene was reduced to a concentration of 0.3 wt%. The silica particles were sprayed with 0.25% MC. The 450 nm and 210 nm particles were sprayed at a ratio of 1:2.4 MC to silica, while the 70 nm silica dispersion concentration was varied at weight ratios of 1:0, 1:0.6, 1:1.2, 1:1.8, and 1:2.4 MC to silica.

Electrospray setup

The electrospray setup used has been described previously.⁴ Briefly, the solution is delivered via syringe pump with the solution in a disposable syringe (1 mL NORM-JECT®) connected by PTFE tubing to a steel needle (Sai Infusion, 20 gauge, 1.5"). High voltage power supplies (Matsusada Precision Inc. RB30-30P) are used to apply voltage to both the steel needle and a steel focusing ring (inner diameter of 2 cm and an outer diameter of 4 cm) located 1 cm above the needle tip. During spray, a silicon wafer is positioned below the needle tip, and clipped to a grounding wire to allow for charge dissipation.

Spray conditions

During the spray, the voltage applied to the needle was 6 kV. The ring voltage was varied from 2.3-3.1 kV to maintain stable Taylor-cone jet sprays. Ambient humidity ranged from 45 and 60% while temperatures remained between 19 and 22 °C, and the substrate was kept at 90 °C using a hotplate. The spray distance was 4 cm, and the material was delivered at a flow rate of 0.1 mL h⁻¹. During the experiments, the spray was first stabilized with a 100 mm diameter Si wafer as a target. To collect the sample for SEM imaging, small pieces of wafer (<1 cm²) were placed on the larger wafer for 40 seconds without pausing the spray. These samples were then mounted directly onto flat aluminum SEM studs using carbon tape.

Characterization

Samples were viewed using a Zeiss Sigma Field Emission Scanning Electron Microscope using both in-lens imaging and backscattering imaging depending on the contrast provided by

the materials. The individual series were measured from these images using imageJ.29

Results and discussion

We perform eDPD simulations to model the dynamics of electrified particle-laden MC droplets undergoing evaporation in flight. The simulation parameters are adjusted to achieve the nanowire formation regime observed in our previous studies.7 We first examine the effect of a single embedded NP on the morphology evolution of the MC droplet. This system represents the dilute solution experiments in which sprayed droplets encompass one or zero particles. The particle size is systematically varied in this study from $R_p = 1$ to $R_p = 6$. This range of particle size is chosen based on the characteristic diameter (approximately 7.6) of nanowire formed from a particlefree droplet (Fig. S3c†). We note that our previous work shows that uncharged MC droplets maintain a spherical shape under solvent evaporation, and no wire formation was observed.⁷ These controls confirm that the deformation is driven by electrostatic interactions.

Initially, the droplet of radius 12 is placed at the center of the simulation box. As evaporation occurs, the solid fraction (including polymer and NPs) of the droplet increases, resulting in an increase in viscosity. Simultaneously, the charge density increases as the total droplet volume decreases. When the electric stress overcomes the surface tension, the droplet deforms and Coulombic fission occurs. This is the classical physical picture of simple fluid electrospray. However, for polymeric fluids or colloidal suspensions, the viscous force also plays a vital role in arresting electrohydrodynamic deformation. Therefore, the competition between viscous and electrostatic forces largely dictates the resulting morphology of the particleladen MC droplet.

Fig. 1 shows the time evolution of the representative run for each particle size. The inclusion of rigid particles has notable effects on the morphology development of MC droplets. Qualitatively, nanowire formation is dominant for droplets with small particles, while large particles suppress the droplet deformation. It is well recognized that electrospray involves various inherent instabilities³⁰ and is a highly stochastic process. In our simulation, the deformation of electrified droplets is sensitively dependent on the spatial distributions of polymer, ion, and particles. Fig. S4† summarizes the final morphologies of the independent runs and demonstrates the variations in the morphology change among the droplets of the same composition. Nevertheless, the systematic simulations confirm that the nanowire shape becomes less well-defined as the particle size increases.

We quantify the droplet deformation by calculating the radius of gyration (R_g) and the relative shape anisotropy (κ^2) . As seen in Fig. 2a, the $R_{\rm g}$ first monotonically decreases in all three cases as the droplets shrink due to solvent evaporation. The spherical shape is well maintained as the values of κ^2 remain close to 0. After the evaporation progress exceeds 50%,

Nanoscale Paper

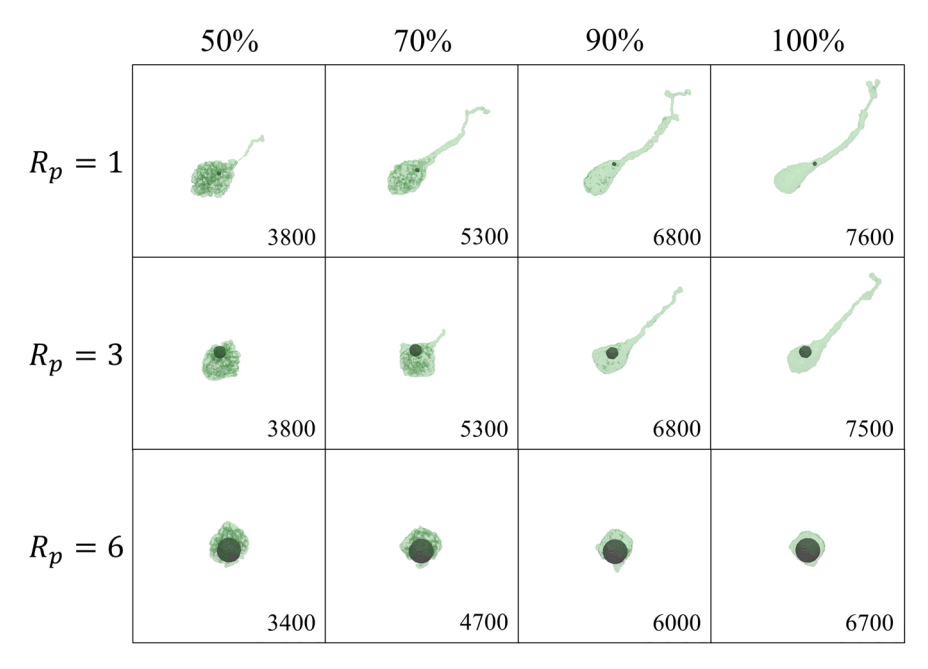


Fig. 1 Dynamic evolution of single-particle droplet morphologies for three particle sizes at four different stages of evaporation marked by the approximate percentage of removed solvent beads. The volume occupied by MC polymer is represented by a transparent green isosurface extracted from a volumetric Gaussian density map. The solid gray spheres are constituent beads of NPs. Solvent, ion, and gas beads are not displayed for clarity. The viewing angles are adjusted so that the directions of droplet deformation are consistent for better comparison. The number in the bottom right of each snapshot indicates the time step at which the simulation snapshot was taken. Notably, the progression of evaporation is not consistent among droplets having particles of different sizes even though a constant evaporation rate is applied.

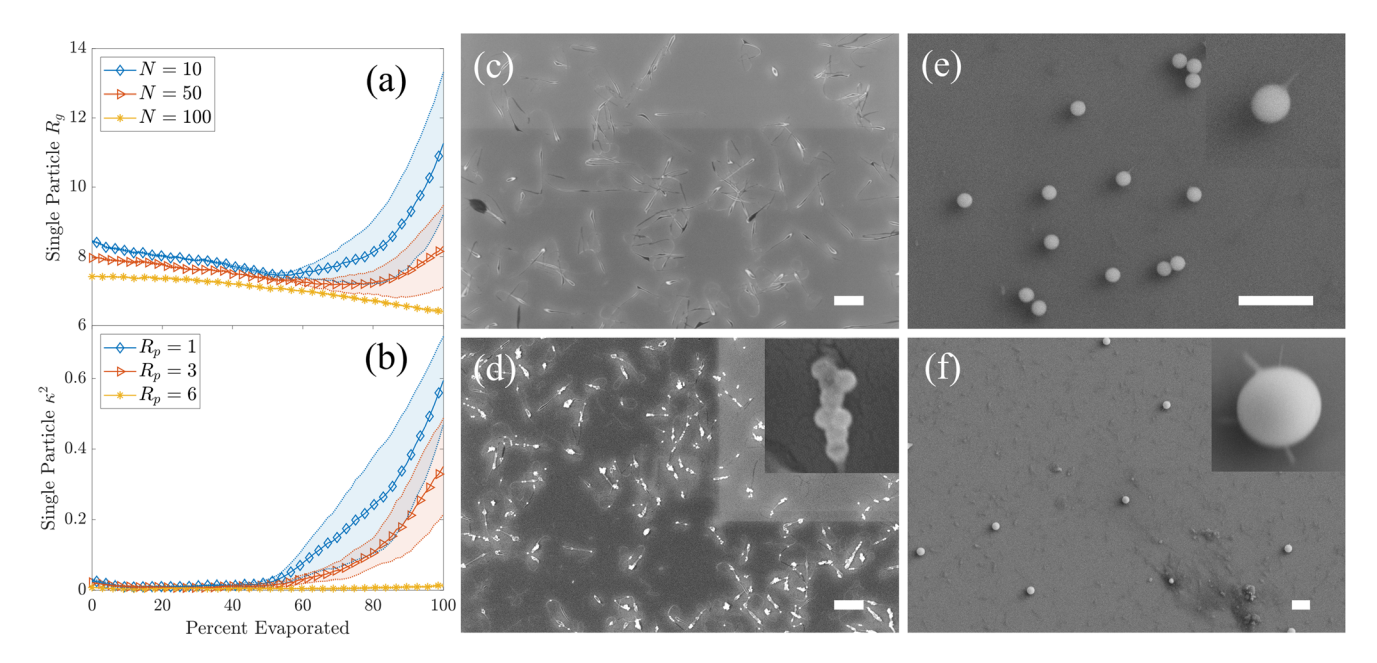


Fig. 2 (a) Radius of gyration and (b) relative shape anisotropy of the droplets containing a single particle of varying radii during evaporation. The progress of evaporation is characterized by the percentage of solvent beads evaporated. The shaded error region represents the standard error of the mean from five independent runs. (c-f) Scanning electron microscope (SEM) images of MC nanowires sprayed at 0.25 wt% (c) without and with (d) 1:0.6 70 nm, (e) 1:2.4 210 nm, (f) 1:2.4 450 nm silica NPs with magnified insets showing the interaction of the NPs and the MC. Scale bars are 1 µm.

the droplets having $R_p = 1$ and $R_p = 3$ particles exhibit deformation. The significant increase in κ^2 in Fig. 2b indicates the pronounced elongation of the droplet into a nanowire.

Remarkably, the droplet ceases to deform as the particle size increases to 6 (see Fig. 1). The decreases in $R_{\rm g}$ and κ^2 of final morphologies confirm that the presence of particle inclusion arrests deformation. The nanowire formation is completely suppressed when the particle size is significantly greater than the characteristic diameter of MC nanowires.

Although the droplets with small particles readily form nanowires, their dynamics have subtle differences from those of particle-free droplets. Due to the significant contrast in mobility imparted by adding a particle, the deformation features the charge-driven jetting of polymer filament (Fig. S5†) and its subsequent growth largely in the transverse direction (see Video S1†). Compared with the particle-free droplets (Fig. S2†), the simulation shows that the particle-induced heterogeneity promotes the tadpole morphology of nanowires. The influences of nonuniform mobility seen here are consistent with those contributing to forming "beads-on-strings" in previous studies.^{7,31} We can confirm this effect experimentally by performing ESD of MC composited with small (70 nm) and large (210 and 450 nm) silica particles (Fig. 2d and e). Based on the particle-free nanowire (Fig. 2c) diameter of 110 ± 30 nm (number of measurements, $N_{\rm m}$ = 66), these particle sizes correspond to $R_p \approx 2$, 7, and 15 in the model. As compared to the micron-length nanowires formed without nanoparticles (Fig. 2c) or with small particles (Fig. 2d), only small filaments with lengths of 100-300 nm were observed in either the 210 (Fig. 2e) or 450 nm (Fig. 2f) particle cases. These arrested morphologies resemble well the ones of $R_p = 6$ droplets seen in Fig. S4.†

To further investigate the effect of NP concentration on nanowire formation, we consider the droplet contains multiple NPs of the smallest size $R_{\rm p}=1$. The numbers of NPs included are N=10, 50, and 100. All other system parameters are the same as in the previous cases. These small NPs can be viewed

as viscosity modifiers, which homogeneously modulate the droplet viscosity. Fig. 3 and S7† confirm that the multi-particle droplets readily form nanowires when the particle concentration is low but resist deformation at high particle concentrations. The dynamic evolution of the morphology of multiparticle droplets more closely resembles that of particle-free droplets (see Fig. S8† for ion distribution and Video S2† for the full dynamics of the droplet). This agreement highlights that the homogeneous viscosity transition underpins nanowire formation. It is apparent from Fig. 4a and b that with an increase in the number of NPs the degree of droplet deformation gradually decreases. Here, the inhibited deformation is readily attributed to an increasing base viscosity of the droplet. A higher concentration of solid particles leads to a higher effective viscosity, continually increasing as the solvent evaporates. Since viscous forces balance electrostatic forces, a uniform increase in droplet viscosity will render smaller deformation and make nanowire formation less likely when Coulombic fission occurs. This effect can also be confirmed experimentally, where adding 70 nm silica nanoparticles results in gradual suppression of the nanowire length after an initial increase due to the addition of extra mass (Fig. 2d and 4e-g). Interestingly, while nanowire formation is suppressed, the size of NP clusters still increases with adding MC as compared to spray without any MC (Fig. S6†). This is likely due to the plasticization of the cluster, allowing for the flattening of the clusters on arrival at the surface.

Lastly, we extend the model to particles with complex topologies, investigating the effect of surface curvature on guiding electrohydrodynamic deformation of MC droplets. We simulate MC droplets with a single embedded particle of shapes

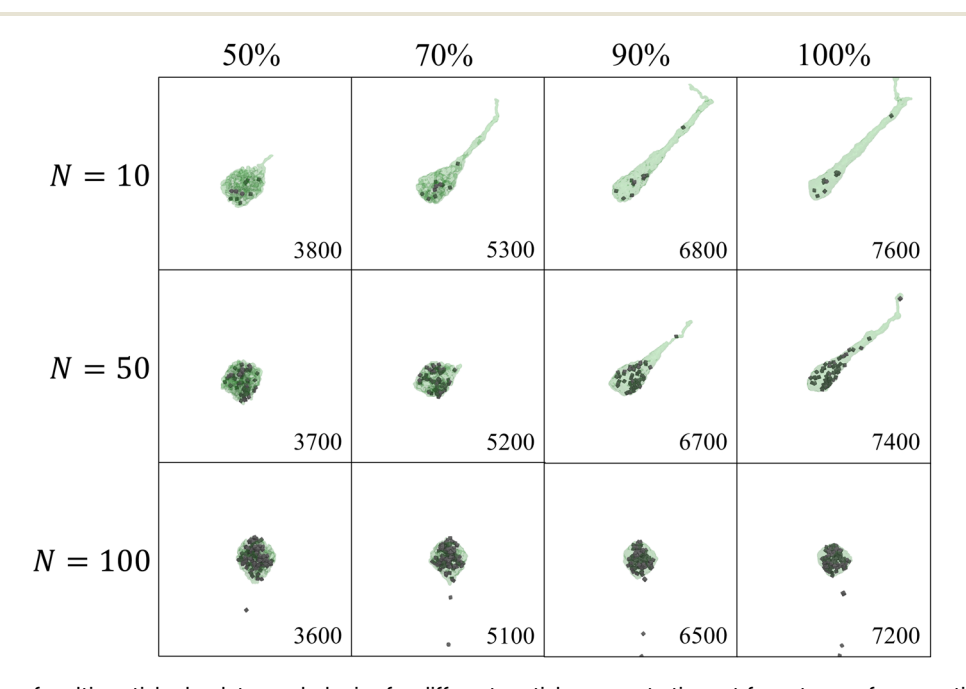


Fig. 3 Time evolution of multi-particle droplet morphologies for different particle concentrations at four stages of evaporation. The presentations of different components are the same as Fig. 1. The view angles were adjusted so that the directions of droplet deformation are consistent for better comparison. The number in the bottom right of each snapshot indicates the time step at which the simulation snapshot was taken.

Nanoscale

20

40 60 Percent Evaporated

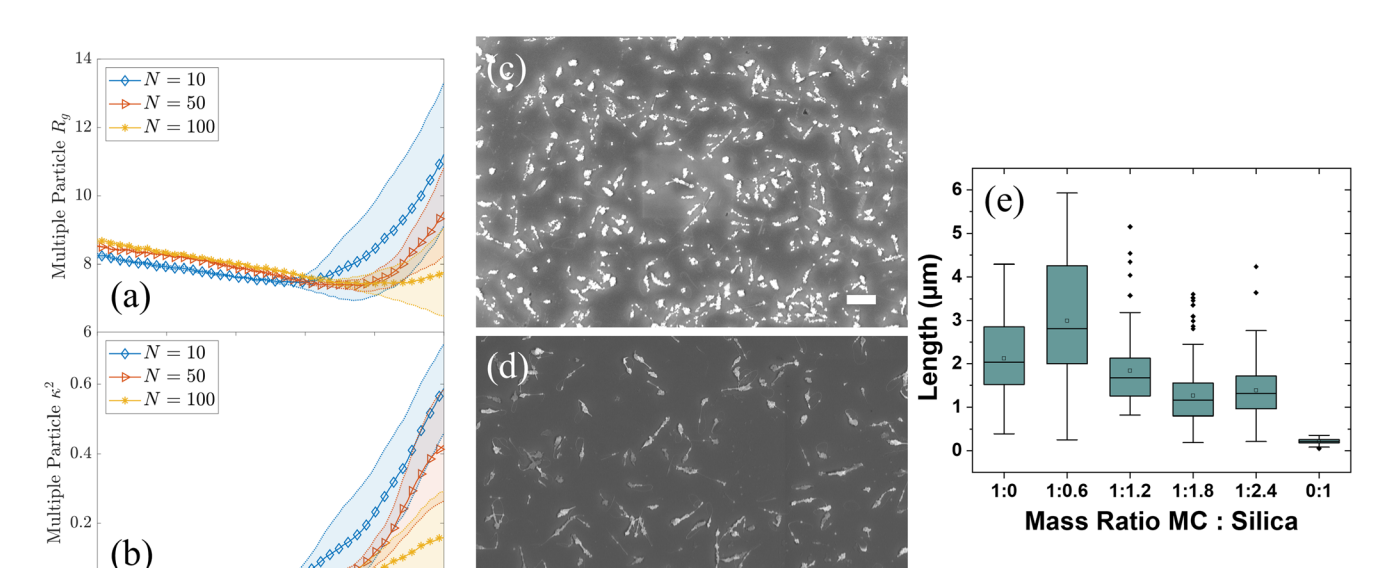


Fig. 4 (a) Radius of gyration and (b) relative shape anisotropy of the multi-particle droplets having a varying number of particles of radius 1 during evaporation. The shaded error region represents the standard error of the mean from independent runs. (c and d) SEM images 0.25 wt% MC sprays at (c) 1:1.2 and (d) 1:2.4 mass ratio with 70 nm silica nanoparticles. Scale bars are 1 μ m. (e) Length measurement extracted from sprays with different ratios of MC and 70 nm silica particles sprayed at 0.25 wt% MC (or 0.6 wt% silica in the pure silica case). The numbers of measurements are $N_m = 79$ for 1:0, $N_m = 46$ for 1:0.6, $N_m = 83$ for 1:1.2, $N_m = 183$ for 1:1.8, $N_m = 99$ for 1:2.4, and $N_m = 138$ for 0:1.

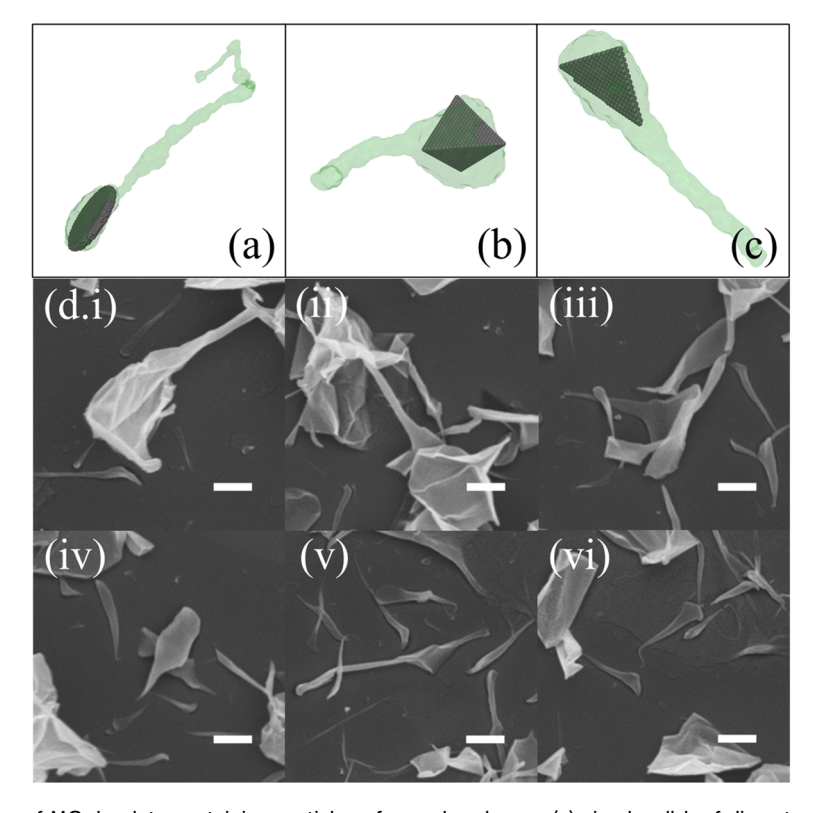


Fig. 5 The final morphologies of MC droplets containing particles of complex shapes: (a) circular disk of diameter 20 and thickness 1, (b) tetrahedron of side length 13, and (c) triangular plate of side length 20 and thickness 1. (d) Subsections of an SEM image of 1 wt% MC sprayed together with 0.3 wt% MXene particles showing wires emitting from the vertices of flakes and flake agglomerates sized large to small (i to vi). Scale bars are 500 nm. The full image along with the image of MXene sprayed alone are available in Fig. S9.†

Paper Nanoscale

including circular disk, tetrahedron, and triangular plate. Notably, these particles are commensurable or larger in size compared with pure MC nanowires. In contrast to large spherical particles that suppress nanowire formation, wires can be readily observed in the presence of anisotropic particles. More interestingly, the simulations show that wires consistently emerge from the structure edges or vertices (Fig. 5a-c). No wires are formed from the extended faces of embedded particles. We speculate that the mechanism of guided nanowire formation with anisotropic particles is the focusing of the electric field at sharp geometries. 32 As a result, regions of high curvature will experience increased electric stress that facilitates the formation of Taylor cone pseudopods.³³ The inclusion of anisotropic particles thus promotes and directs the electrohydrodynamic deformation of spray droplets. This behavior is consistent with observations in electrospray mass ionization that the sharp vertex of a graphene flake can enable the ionization of otherwise incompatible fluids.³⁴ We further investigate the effects of particle shape through electrospray experiments. Ti₃C₂T_x was selected for this study because it is the most studied and best understood MXene material. Ti₃C₂T_x has high electrical conductivity, stability, and is promising for electrochemical energy storage. In addition, there have been a variety of studies focused on its rheology in solution.³⁵ This led us to believe that this MXene would be the best starting material to test with. However, there are more than 30 stoichiometric MXene compositions and an infinite number of solidsolution MXenes, all with their own properties and applications.36,37 Generally, all MXenes have similar rheological properties, so our preliminary testing with Ti₃C₂T_x implies that similar results could be obtained with other MXenes, and this will be further tested in future studies. Other 2D materials have different properties, especially in context with their solution processibility. MXenes are a unique class that require no additives (e.g., surfactants) to be dispersible in water.³⁸ This is in stark contrast to graphene, h-BN, and other 2D materials that resist dispersion in water without advanced processing. Through incorporating MXene flakes of disperse sizes, it was observed in Fig. 5d that the formation of MC wires is indeed from the vertices of the flakes. The excellent agreement between simulation and experimental results demonstrates the efficacy of our model in predicting the electrohydrodynamics of multiphase and multicomponent droplets.

Conclusion

We apply both computer simulations and experiments to study the influences of nanoparticle inclusions on the deformation of electrified polymer droplets. The results of deposit morphology, quantified by the radius of gyration, relative shape anisotropy, and aspect ratio, show that particle size and concentration significantly affect droplet morphology evolution. For single-particle systems, the increase in particle size decreases the degree of deformation and reduces the consistency in nanowire formation. It was observed that increased mobility

inhomogeneity in the presence of nanoparticles facilitates tadpole morphologies compared to particle-free droplets. No deformation was observed when the particle size was significantly larger than the characteristic diameter of particle-free wires. Increasing concentrations of small particles also suppress droplet deformation. The impact of surface curvature induced by particles with complex geometries was also explored, showing consistent wire formation particle edges and vertices. The findings provide critical insight into physical mechanisms that govern morphology development in multiphase, multicomponent droplets far from equilibrium. The results also pave the way for employing the coarse-grained ESD model and MC nanowires for increasingly advanced nanocomposites in future work.

Conflicts of interest

The authors declare no conflict of interest.

Acknowledgements

J. M. B. and X. Y. acknowledge funding from the National Science Foundation for supporting this work through award 1939362. M. J. G., R. M. V., and J. P. S. acknowledge funding from the National Science Foundation through award 1911518.

References

- 1 A. Jaworek and A. T. Sobczyk, Electrospraying route to nanotechnology: An overview, *J. Electrost.*, 2008, **66**(3–4), 197–219.
- 2 S. Kavadiya and P. Biswas, Electrospray deposition of biomolecules: Applications, challenges, and recommendations, *J. Aerosol Sci.*, 2018, 125, 182–207.
- 3 K. Toth, C. O. Osuji, K. G. Yager and G. S. Doerk, Electrospray deposition tool: Creating compositionally gradient libraries of nanomaterials, *Rev. Sci. Instrum.*, 2020, **91**(1), 013701.
- 4 L. Lei, D. A. Kovacevich, M. P. Nitzsche, J. Ryu, K. Al-Marzoki, G. Rodriguez, L. C. Klein, A. Jitianu and J. P. Singer, Obtaining Thickness-Limited Electrospray Deposition for 3D Coating, ACS Appl. Mater. Interfaces, 2018, 10(13), 11175–11188.
- 5 W. C. Yan, J. Xie and C. H. Wang, Electrical Field Guided Electrospray Deposition for Production of Gradient Particle Patterns, ACS Appl. Mater. Interfaces, 2018, 10(22), 18499– 18506.
- 6 Y. Zhu and P. R. Chiarot, Directed assembly of nanomaterials using electrospray deposition and substrate-level patterning, *Powder Technol.*, 2020, 364, 845–850.
- 7 L. Lei, S. Chen, C. J. Nachtigal, T. F. Moy, X. Yong and J. P. Singer, Homogeneous gelation leads to nanowire forests in the transition between electrospray and electrospinning, *Mater. Horiz.*, 2020, 7(10), 2643–2650.

8 E. Castillo-Orozco, A. Kar and R. Kumar, Electrospray mode transition of microdroplets with semiconductor nano-

Nanoscale

particle suspension, Sci. Rep., 2017, 7(1), 5144. 9 R. Sridhar and S. Ramakrishna, Electrosprayed nanoparticles for drug delivery and pharmaceutical applications,

- Biomatter, 2013, 3(3), e24281.
- 10 J. A. Tapia-Hernandez, P. I. Torres-Chavez, B. Ramirez-Wong, A. Rascon-Chu, M. Plascencia-Jatomea, C. G. Barreras-Urbina, N. A. Rangel-Vazquez and F. Rodriguez-Felix, Micro- and nanoparticles by electrospray: advances and applications in foods, J. Agric. Food Chem., 2015, 63(19), 4699-4707.
- 11 R. A. Green-Warren, L. Bontoux, N. M. McAllister, D. A. Kovacevich, A. Shaikh, C. Kuznetsova, M. Tenorio, L. Lei, A. A. Pelegri and J. P. Singer, Determining the Self-Limiting Electrospray Deposition Compositional Limits for Mechanically Tunable Polymer Composites, ACS Appl. Polym. Mater., 2022, 4(5), 3511-3519.
- 12 L. Lei, A. R. Gamboa, C. Kuznetsova, S. Littlecreek, J. Wang, Q. Zou, J. D. Zahn and J. P. Singer, Self-limiting electrospray deposition on polymer templates, Sci. Rep., 2020, 10(1), 17290.
- 13 D. A. Kovacevich, L. Lei, D. Han, C. Kuznetsova, S. E. Kooi, H. Lee and J. P. Singer, Self-Limiting Electrospray Deposition for the Surface Modification of Additively Manufactured Parts, ACS Appl. Mater. Interfaces, 2020, 12(18), 20901-20911.
- 14 G. C. Rutledge and S. V. Fridrikh, Formation of fibers by electrospinning, Adv. Drug Delivery Rev., 2007, 59(14), 1384-1391.
- 15 G. S. Jagdale, M. H. Choi, N. P. Siepser, S. Jeong, Y. Wang, R. X. Skalla, K. Huang, X. Ye and L. A. Baker, Electrospray deposition for single nanoparticle studies, Anal. Methods, 2021, 13(36), 4105-4113.
- 16 M. Naguib, M. W. Barsoum and Y. Gogotsi, Ten Years of Progress in the Synthesis and Development of MXenes, Adv. Mater., 2021, 33(39), 2103393.
- 17 R. D. Groot and P. B. Warren, Dissipative particle dynamics: Bridging the gap between atomistic and mesoscopic simulation, J. Chem. Phys., 1997, 107(11), 4423-4435.
- 18 P. Espanol, Hydrodynamics from dissipative particle dynamics, Phys. Rev. E: Stat. Phys., Plasmas, Fluids, Relat. Interdiscip. Top., 1995, 52(2), 1734-1742.
- 19 R. D. Groot, Electrostatic interactions in dissipative particle dynamics-simulation of polyelectrolytes and anionic surfactants, J. Chem. Phys., 2003, 118(24), 11265-
- 20 M. Gonzalez-Melchor, E. Mayoral, M. E. Velazquez and J. Alejandre, Electrostatic interactions in dissipative particle dynamics using the Ewald sums, J. Chem. Phys., 2006, **125**(22), 224107.
- 21 K. A. Terron-Mejia, R. Lopez-Rendon and A. G. Goicochea, Electrostatics in dissipative particle dynamics using Ewald sums with point charges, J. Phys.: Condens. Matter, 2016, 28(42), 425101.

- 22 A. P. Thompson, H. M. Aktulga, D. S. Bolintineanu, W. M. Brown, P. S. Crozier, P. J. in 't Veld, A. Kohlmeyer, S. G. Moore, T. D. Nguyen, R. Shan, M. J. Stevens, J. Tranchida, C. Trott and S. J. Plimpton, LAMMPS - a flexible simulation tool for particle-based materials modeling at the atomic, meso, and continuum scales, Comput. Phys. Commun., 2022, 271, 108171.
- 23 S. Qin and X. Yong, Interfacial adsorption of pH-responsive polymers and nanoparticles, Soft Matter, 2017, 13(30), 5137-5149.
- 24 S. Qin, J. Kang and X. Yong, Structure and Dynamics of Stimuli-Responsive Nanoparticle Monolayers at Fluid Interfaces, Langmuir, 2018, 34(19), 5581-5591.
- 25 P. Nikunen, I. Vattulainen and M. Karttunen, Reptational dynamics in dissipative particle dynamics simulations of polymer melts, Phys. Rev. E: Stat., Nonlinear, Soft Matter Phys., 2007, 75(3 Pt 2), 036713.
- 26 X. Yong, O. Kuksenok, K. Matyjaszewski and A. C. Balazs, Harnessing interfacially-active nanorods to regenerate severed polymer gels, Nano Lett., 2013, 13(12), 6269-6274.
- 27 X. Yong, Modeling the Assembly of Polymer-Grafted Nanoparticles at Oil-Water Interfaces, Langmuir, 2015, 31(42), 11458-11469.
- 28 C. E. Shuck, K. Ventura-Martinez, A. Goad, S. Uzun, M. Shekhirev and Y. Gogotsi, Safe Synthesis of MAX and MXene: Guidelines to Reduce Risk During Synthesis, ACS Chem. Health Saf., 2021, 28(5), 326-338.
- 29 J. Schindelin, I. Arganda-Carreras, E. Frise, V. Kaynig, M. Longair, T. Pietzsch, S. Preibisch, C. Rueden, S. Saalfeld, B. Schmid, J.-Y. Tinevez, D. J. White, V. Hartenstein, K. Eliceiri, P. Tomancak and A. Cardona, Fiji: an open-source platform for biological-image analysis, Nat. Methods, 2012, 9(7), 676-682.
- 30 A. M. Gañán-Calvo, J. M. López-Herrera, M. A. Herrada, A. Ramos and J. M. Montanero, Review on the physics of electrospray: From electrokinetics to the operating conditions of single and coaxial Taylor cone-jets, and AC electrospray, J. Aerosol Sci., 2018, 125, 32-56.
- 31 B. Almeria, W. Deng, T. M. Fahmy and A. Gomez, Controlling the morphology of electrospray-generated PLGA microparticles for drug delivery, J. Colloid Interface Sci., 2010, 343(1), 125-133.
- 32 J. D. Jackson, in Classical Electrodynamics, Wiley, New York, NY, 3rd edn, 1999.
- 33 M. Wilm, Principles of electrospray ionization, Mol. Cell. Proteomics, 2011, 10(7), M111 009407.
- 34 B. Xia, Y. Gao, B. Ji, F. Ma, L. Ding and Y. Zhou, Analysis of Compounds Dissolved in Nonpolar Solvents Electrospray Ionization on Conductive Nanomaterials, J. Am. Soc. Mass Spectrom., 2018, 29(3), 573-580.
- 35 B. Akuzum, K. Maleski, B. Anasori, P. Lelyukh, N. J. Alvarez, E. C. Kumbur and Y. Gogotsi, Rheological Characteristics of 2D Titanium Carbide (MXene) Dispersions: A Guide for Processing MXenes, ACS Nano, 2018, 12(3), 2685-2694.

Paper Nanoscale

- 36 M. Han, K. Maleski, C. E. Shuck, Y. Yang, J. T. Glazar, A. C. Foucher, K. Hantanasirisakul, A. Sarycheva, N. C. Frey, S. J. May, V. B. Shenoy, E. A. Stach and Y. Gogotsi, Tailoring Electronic and Optical Properties of MXenes through Forming Solid Solutions, J. Am. Chem. Soc., 2020, 142(45), 19110-19118.
- 37 A. VahidMohammadi, J. Rosen and Y. Gogotsi, The world of two-dimensional carbides and nitrides (MXenes), Science, 2021, 372(6547), eabf1581.
- 38 K. Maleski, V. N. Mochalin and Y. Gogotsi, Dispersions of Two-Dimensional Titanium Carbide MXene in Organic Solvents, Chem. Mater., 2017, 29(4), 1632-1640.